UCLA

UCLA Previously Published Works

Title

Morphology of the 12 Micron Seyfert Galaxies. II. Optical and Near-Infrared Image Atlas**Based on observations collected at the Calar Alto Observatory, the Cerro Tololo Interamerican Observatory, the European Southern Obsevatory, the Gornergrat Infra...

Permalink

Journal

ISSN

Authors

Hunt, LK
Malkan, MA
Rush, B
et al.

Publication Date

1999-12-01

DOI

Peer reviewed

Morphology of the $12\,\mu$m Seyfert Galaxies: II. Optical and Near-Infrared Image Atlas[1]

L. K. Hunt

C. A. I. S. M. I. - C. N. R.
Largo E. Fermi 5, I-50125 Firenze, Italy
Electronic mail: hunt@arcetri.astro.it

M. A. Malkan

University of California
Department of Astronomy, 405 Hilgard Ave.,
Los Angeles, CA, U.S.A. 90095-1562
Electronic mail: malkan@bonnie.astro.ucla.edu

B. Rush

University of California
Department of Astronomy, 405 Hilgard Ave.,
Los Angeles, CA, U.S.A. 90095-1562
Electronic mail: rush@bonnie.astro.ucla.edu

M. D. Bicay

S.I.R.T.F. Science Center,
Infrared Processing and Analysis Center,
Pasadena, CA, U.S.A.
Electronic mail: michael.d.bicay@jpl.nasa.gov

B. O. Nelson

Infrared Processing and Analysis Center,
Pasadena, CA, U.S.A.
Electronic mail: nelson@ipac.caltech.edu

R. M. Stanga

Università di Firenze
Istituto di Astronomia, Largo E. Fermi 5, I-50125 Firenze, Italy
Electronic mail: stanga@arcetri.astro.it

and

W. Webb

University of California
Department of Astronomy, 405 Hilgard Ave.,
Los Angeles, CA, U.S.A. 90095-1562
Electronic mail: webb@bonnie.astro.ucla.edu

ABSTRACT

We present 263 optical and near-infrared (NIR) images for 42 Seyfert 1s and 48 Seyfert 2s, selected from the Extended $12\,\mu$m Galaxy Sample. Elliptically-averaged profiles are derived from the images, and isophotal radii and magnitudes are calculated from these. We also report virtual aperture photometry, that judging from comparison with previous work, is accurate to roughly $0.05\,$mag in the optical, and $0.07\,$mag in the NIR. Our B-band isophotal magnitude and radii, obtained from ellipse fitting, are in good agreement with those of RC3. When compared with the B band, V, I, J, and K isophotal diameters show that the colors in the outer regions of Seyferts are consistent with the colors of normal spirals. Differences in the integrated isophotal colors and comparison with a simple model show that the active nucleus+ bulge are stronger and redder in the NIR than in the optical. Finally, roughly estimated Seyfert disk surface brightnesses are significantly brighter in B and K than those in normal spirals of similar morphological type.

Subject headings: Atlases; galaxies: Seyfert; galaxies: active; galaxies: photometry; infrared: galaxies

1. Introduction

Many studies have been devoted to the broad-band optical and near-infrared (NIR) properties of Seyfert nuclei and the galaxies that contain them. Early photographic work was aimed at the large-scale morphology of the host galaxies, and found that, together with a surplus of disturbed and interacting systems, there may be a preponderance of annular structures (Adams 1977). Unusually high outer ring fractions in Seyferts were also noted by Simkin, Su, & Schwarz (1980), who suggested that the patterns in Seyfert disk/ring morphology they observed could be explained by the consequences of radial gas inflow. Peculiar or disturbed morphologies were also found in roughly a third of the Seyfert sample studied by MacKenty (1990).

Other early work noted a strong preference for peculiar blue nuclei to reside in barred or weakly-barred spirals (Sersic & Pastoriza 1967; Sersic 1973), but this result was disputed by Heckman (1978) who found that such nuclei occurred with equal frequency in barred and unbarred systems. This was only the beginning of the search for bars in Seyferts, thought to be responsible via large-scale gravitational torques for fueling active nuclei (e.g., Shlosman, Begelman, & Frank 1990). The latest studies show that while starbursts are almost always barred (Hunt & Malkan 1999), Seyferts are barred with the same frequency as normal spirals (McLeod & Rieke 1995; Ho, Filippenko, & Sargent (1997); Mulchaey & Regan 1997). Recently, though, it has been claimed that bars and non-axisymmetric distortions occur more frequently in Seyfert 2s than 1s (Maiolino et al. 1997). Small-scale gaseous bars, or the "bars-within-bars" scenario proposed by Shlosman, Frank, & Begelman (1989) may be more relevant to the problem of nuclear fueling, because large-scale galactic bars cannot drive gas inwards on the small spatial scales of the galactic nucleus. Indeed, NIR Hubble Space Telescope observations reveal a dusty nuclear bar about 80 pc long in a nearby Seyfert (Maiolino et al. 1998).

Later work was aimed at quantifying the broad-band colors of the underlying galaxy and the Seyfert nucleus itself. Although colors of host galaxies have been extensively studied, they are still a subject of debate. Yee (1983) and MacKenty (1990) found optical colors of Seyfert hosts to be similar to normal spirals, while bluer integrated colors were found by Granato et al. (1993), and redder circumnuclear colors by Kotilainen & Ward (1994). NIR colors are equally controversial: Danese et al. (1992), Kotilainen & Ward (1994), and Alonso-Herrero, Ward, & Kotilainen (1996) found normal $J - H$ colors, but red $H - K$, and attributed these to hot dust and enhanced circumnuclear star formation. Normal $H - K$ colors, instead, were found by Hunt & Giovanardi (1992) and Hunt et al. (1997), who corrected the observed colors for redshift. Hunt et al. argued that the omission of this correction could explain the red $H - K$ colors found by earlier work.

Photometric studies of the Seyfert nucleus are hampered by the difficulty in separating the unresolved nuclear component from the underlying galaxy. Nuclear amplitudes can be obtained by fitting a point-source to the radial profiles (Yee 1983; McLeod & Rieke 1995), or by more sophisticated decomposition techniques which fit one-dimensional brightness profiles with bulge, disk, and nuclear contributions (Kotilainen et al. 1992a; Zitelli et al. 1993). It was suggested that the nuclei in type 1 Seyferts are much bluer (optically) than type 2 nuclei, and that the ratio of nuclear-to-galaxy luminosity is much larger in type 1s (Yee 1983). This last appears to be true also in the NIR, since the starlight contribution in a given observing aperture was shown to be much larger in Seyfert 2s than in type 1s (Alonso-Herrero et al. 1996).

In this paper, we present new optical and NIR images of Seyferts that can help understand and perhaps resolve some of the questions and controversies outlined above (see also Peletier et al. 1999). These data are part of a larger study, aimed at investigating structural features in order to assess whether Seyfert galaxies are, like their energetic nuclei, peculiar. The first paper in this series (Hunt & Malkan 1999; hereafter Paper I) consisted of a statistical investigation of the morphological properties of the 891 galaxies in the $12\,\mu$m Galaxy Sample (Rush, Malkan, & Spinoglio 1993), including normal spirals, starburst/HII galaxies, LINERs, and Seyferts. We found that HII/starburst galaxies have a very high bar fraction, but that Seyferts and LINERs have the same frequency of bars as normal spirals. Unlike starbursts, however, LINERs and Seyferts show rings significantly more often than normal galaxies or starbursts: LINERs have elevated rates of inner rings, and Seyferts have outer ring fractions several times those in normal spirals. Many of these results corroborate the suggestions of earlier work (e.g., Adams

1977; Simkin et al. 1980), but clearly a quantitative analysis of digital images is needed.

Here we present an optical and NIR image atlas of 90 $12\,\mu$m-selected Seyferts, together with results from elliptical isophote fitting. This set of 263 optical and NIR images for 42 Seyfert 1s and 48 Seyfert 2s comprises 80% of the $12\,\mu$m Seyfert Sample, and is one of the largest image databases of Seyfert galaxies ever compiled. Selection criteria of the Extended $12\,\mu$m Galaxy Sample (E12GS) are described in Rush, Malkan, & Spinoglio (1993). The following section evaluates how well the morphological properties of the observed sample represent the complete $12\,\mu$m Seyfert Sample. Section 3 describes the observations, data reduction, and photometric calibrations, as well as the aperture photometry. Elliptical isophote fitting is presented in §4, and the properties of the isophotal radii and magnitudes in *BVIJHK* are analyzed in §5. Section 6 discusses the Seyfert disk surface brightnesses, estimated from an exponential fit of the outer profiles. An analysis of the properties of bars and lenses, in terms of their isophotal characteristics, among the different bands and between the two Seyfert types is deferred to a companion paper.

2. Properties of the Observed Sample

We are interested in the conformity of the observed subsample to the morphological properties of the $12\,\mu$m Seyferts as a whole. The presentation of the data in the following section is therefore anticipated here by a preview of the morphological characteristics of the observed subsample of 90 galaxies. It turns out that median morphological types, and bar and ring fractions of the $12\,\mu$m Seyferts in this paper are very similar to the complete sample studied in Paper I. Seyfert 1s have a median type of T = 1 (Sa), and Seyfert 2s T = 2 (Sab). 65% of the Seyfert 1s are strongly (SB) or weakly (SAB) barred, as are 56% of the Seyfert 2s. 40% of the Seyfert 1s and 35% of the Seyfert 2s have outer or pseudo-outer rings, while 39% (2s) to 45% (1s) have inner rings. Even the number ratio of type 2s to type 1s (48/42) is similar to that in the complete sample (63/53). Therefore, we conclude that the observed subsample provides a good representation of the $12\,\mu$m Seyferts as a whole, at least in terms of the morphology we are studying.

The median recession velocities for the two types are comparable, but with Seyfert 1s being generally farther away (median $z = 0.021$) than type 2s (median $z = 0.015$). This difference, although moderate, could cause spurious differences to emerge in type comparisons, and will be taken into account in the subsequent analyses.

3. Observations, Reduction, and Photometry

Images of the sample galaxies were acquired over the course of several observing campaigns at six different observatories: Calar Alto[2], CTIO[3], ESO[4], Lick[5], NOT[6], and TIRGO[7]. Observations were performed with seven telescopes, five optical cameras, and three infrared ones. Details of the observing runs and camera characteristics are given in Table 1. All filters are standard broad-band, and, when necessary, converted during calibration to well-defined photometric systems. Image reduction was performed in the IRAF environment[8], together with the STSDAS package[9].

3.1. Optical Data Reduction and Calibration

Standard methods were used to reduce the optical images. First, the bias was subtracted, using when possible, the extended register overscan region. If not available, separate bias frames were acquired at the beginning and end of the night, and the average of these was used for subtraction. If necessary, dark frames at the same exposure time of the science

Table 1

Observing Runs and Camera Characteristics

Observatory	Telescope	Year	Camera	Pixels[a]	Filters	Code
Lick	1-m	1990	TI500	0.54	BI	L90
Lick	1-m	1993	Ford 2048×2048 (binned)	0.37	V	L93
CTIO	0.91-m	1992	TK1024 (binned)	0.792	BVI	C92
ESO	Danish 1.54-m	1992	TK1024	0.38	BVI	E
ESO	MPI 2.2-m	1992	IRAC2	0.49	JHK	I2
TIRGO	1.5-m	1992-93	ARNICA	0.97	JHK	T
Calar Alto	1.23-m	1993	TK510×510	0.567	VI	CA
Lick	1-m	1993-94	KCAM	0.50	K	LK
NOT	2.56-m	1995-96	ARNICA	0.546	JHK	N

[a]In units of arcsec.

frames were also subtracted. Pixel-to-pixel and large-scale spatial variations in the cameras+detectors were corrected for with flat-field frames, acquired during twilight. These were in most cases the combination of dome and sky flats, although in some cases, only sky (ESO) or dome (Calar Alto) flats were used. Cosmic rays were corrected for by the *cosmicrays* algorithm in the IRAF CCD reduction package, and bad columns with linear interpolation (*fixpix*). The sky level was determined by averaging the median (over 5×5 pixel boxes) of several (> 8–10) empty sky areas in the full-format CCD frame.

The reduced images were then calibrated with observations, obtained throughout the various nights, of standard stars taken from the lists of Landolt (1983, 1992). Each photometric measurement was the difference of a central aperture, typically 5 times the FWHM of the point-spread function (PSF), and a concentric, but larger, sky annulus. For each filter, a linear regression was performed on the run of zero points with airmass, and when necessary to derive a color transformation, the residuals were fit to intrinsic color. In some cases (Lick), such a procedure was not possible and mean extinction and color terms were applied. We estimate the formal photometric accuracy, as judged from the standard deviation of the nightly standard stars, to be 0.02–0.03 mag or better for the Calar Alto, CTIO, and ESO data; 0.05 mag for the Lick 1993 data; and roughly 0.10–0.12 mag for the Lick 1990 run.

3.2. Near-Infrared Data Reduction and Calibration

All three NIR cameras are based on 256×256 HgCdTe arrays (NICMOS3), and are described in more detail by Lisi et al. (1996: ARNICA) and Hunt et al. (1996: ARNICA); Moorwood et al. (1992: IRAC2); and Nelson et al (1997: KCAM). In the ESO, TIRGO, and NOT campaigns, galaxies were observed by alternating source and adjacent empty sky exposures, usually beginning and ending with a sky frame, and integrating $\sim 1^m$ in each position. Typical total integration times were 5^m, although the NOT K-band observations were usually twice that. All three cameras employed a double-sampling read-out algorithm, so that the bias level was automatically subtracted. The short on-chip integration times (10–30s) used to prevent saturation from the sky emission obviated the need for dark-current subtraction. Flat fields for each object exposure were obtained by averaging the sky frames acquired immediately before and after it, after removal of any stars in the sky frames. For the TIRGO campaign, these were used directly. For the ESO (in JHK) and the NOT (in K only) campaigns, the average sky frame was first subtracted from the object exposure, then the difference divided by a differential flat field[10] obtained independently. The (typically five) flat-fielded expo-

---

[10]The normalized difference of a uniformly-illuminated frame and a dark one.

sures were cleaned for bad pixels by interpolating a bad-pixel mask, then registered, and combined, using a clipping procedure that relied on the (known) noise characteristics of the cameras. Before combination, each exposure was rescaled to a common median level by adding the appropriate constant. The final step was the subtraction of the background that, as for the optical images, was determined in empty sky regions by averaging the medians within several 5×5 pixel boxes.

For the Lick KCAM campaign, the following procedure was used: each galaxy was exposed at seven different positions on the chip. A sky image was constructed for each position by taking the median of the remaining six images. Each object image was then sky subtracted and corrected for the flat-field, using dome flats taken at the end of each night. These frames were then registered and combined, as above.

The NIR images at ESO, NOT, and TIRGO were calibrated by observing stars from the UKIRT Faint Standard List (Casali & Hawarden 1992); at Lick, they were calibrated with stars from Elias et al. (1982). As in the optical, each photometric measurement was the difference of a central aperture, roughly 5 times the FWHM of the PSF, and a concentric larger annulus which measured the sky. For each run at ESO, NOT, and TIRGO, a fit for the atmospheric extinction coefficient and nightly zero points was performed, assuming that the extinction remained constant from night to night, but allowing the zero points (at unit airmass) to vary. At Lick with KCAM, mean extinction coefficients were used, and only the zero points were fit. We found no evidence for a color transformation between the filter+HgCdTe camera combination and the InSb UKIRT Faint Star magnitudes (but see Hunt et al. 1998). Judging from the scatter of the standard star observations, the formal photometric accuracy of the NIR data is roughly 0.02 mag (JHK, ESO and NOT 1996), 0.03 mag (K, Lick), 0.05 mag (JHK, TIRGO), and 0.06–0.14 mag (JHK, NOT 1995).

3.3. Quality Assessment

Figure 1 shows for each of the 90 galaxies an image and an elliptically-averaged profile (discussed in §4) with radial runs of ellipticity, position angle, and the $\sin 4\theta$ and $\cos 4\theta$ coefficients, A_4 and B_4. The virtual aperture photometry, isophotal magnitudes and radii (discussed in §5), and central surface brightnesses (discussed in §6), are given in Table 2, whose entries are as follows:

Column 1) Seyfert type (integer).
Column 2) Source name or names. An asterix signifies that the (radially varying) longer-wavelength best-fit ellipses were used to derive the isophotal parameters.
Column 3) Morphological type (NED, RC3).
Column 4) Redshift (NED).
Column 5) Filter band.
Column 6–8) Aperture photometry with aperture diameters of 10, 20, and 30 arcsec, respectively.
Column 9) Magnitude integrated to the isophotal radius.
Column 10) Isophotal radius in arcsec, evaluated at an isophote of $25\,\mathrm{mag\,arcsec^{-2}}$ in B; $24\,\mathrm{mag\,arcsec^{-2}}$ in V; $23\,\mathrm{mag\,arcsec^{-2}}$ in I; $22\,\mathrm{mag\,arcsec^{-2}}$ in J; $21.5\,\mathrm{mag\,arcsec^{-2}}$ in H; and $21\,\mathrm{mag\,arcsec^{-2}}$ in K. Radii marked with ^{x} are extrapolated to the isophote, instead of interpolated.
Column 11) Central surface brightness ($\mathrm{mag\,arcsec^{-2}}$) obtained by fitting an exponential to the outer profile.
Column 12) Observing run code (see Col. 7 of Table 1). The code is "X" for two galaxies, NGC 2639 and NGC 3227, and signifies images which were not acquired in the context of an observing run. J and K images for NGC 2639 were taken at Palomar, and for NGC 3227 at Mt. Hopkins.

It can be seen from the Table 2 that the wavelength coverage in the atlas is not uniform. 64 of the 90 galaxies observed have a V-band image, and this is the band for which we have the most sources. 60 have a K-band image, and 35 (different sets of) objects have VK and JK. In each of the remaining optical and NIR bands, the wavelength coverage is similar, with images for between 30 and 40 objects in each band $BIJH$. Moreover, for each wavelength combination (e.g., BV, BI, BVI, VK, JK, JHK), there are 30 or more objects. Consequently, the statistics should be sufficient for a detailed multiwaveband analysis.

To judge the effective spatial resolution of the atlas, we have measured the PSFs of stars in the full-format CCD images (as opposed to the truncated versions shown in Fig. 1). The median full-width-half-maximum (FWHM) of the measured PSFs is 2.0 arcsec in B, 2.2 in V, 1.9 in I, 1.4 in J and H, and 1.5 arcsec in K. Only 20 images of 263 have FWHM $>$

3.0 arcsec. At the median redshifts of our sample (assuming $H_0 = 75$ km/s/Mpc), 2 arcsec corresponds to a resolution of 600-800 pc. Given that typical bulge effective diameters in active galaxies are two–three times this (Hunt et al. 1999), such resolution should be more than adequate to separate the nuclear light from the bulge.

The photometry in this paper can be checked by comparison with previous results. In the optical, we have relied on the variability study by Winkler et al. (1992), conducted with a photometer, with which we have 8 galaxies in common, and on the imaging study by Kotilainen, Ward, & Williger (1993) with which we share 13. If we omit from the comparison IC 4329A which is known to vary in the optical (Winge et al. 1996), our photometry is in good agreement with both groups, with a mean difference (*us - them* over 8-10 data points) of -0.04 ± 0.02 mag in B, 0.04 ± 0.07 in V, and 0.075 ± 0.04 in I relative to Winkler et al., and (*us - them* over 12-20 data points) -0.04 ± 0.06 mag in B, -0.02 ± 0.15 in V, and 0.07 ± 0.06 in I relative to Kotilainen et al. Three galaxies (NGC 4151, NGC 4593, 3C120) contribute more than 0.2 mag to the latter comparison in V, one of which is known to vary in the NIR (NGC 4151, McAlary et al. 1983). Without these, we have -0.002 ± 0.04 over 14 data points. We also have compared our photometry for NGC 1068 with the CCD study of Schild, Tresch-Fienberg, & Huchra (1985), and find excellent agreement (over the 10, 20, and 30 arcsec apertures reported here) with a mean difference (*us - them*) of -0.02 ± 0.006 mag.

Comparison with other NIR studies is more problematic than in the optical for several reasons outlined below. Nevertheless, several of our objects have been observed by other authors and, for the studies which have the most overlap (10 each with Balzano & Weedman 1981 and Kotilainen et al. 1992a; 14 galaxies with McAlary et al. 1983; 36 with Spinoglio et al. 1995), we have compared our photometry with theirs. In no case do we find significant systematic deviations; in all cases the rms difference is 0.15–0.25 mag. One possible reason for such a large scatter may be differences in the filter+detectors (Bessell & Brett 1988), a problem especially for the red nuclei in Seyferts. Indeed, the observed rms scatter is reduced by roughly 40% when only $J - K < 1.9$ are considered. Another contributing factor may be the limited chopper throw (typically a few to several tens of arcsecs) used to effect the sky subtraction in single-element photometry,

since the mean difference *us – them* tends to be negative. Small apertures and consequent difficulties with centering and seeing constitute another problem; the scatter in all bands is reduced by a factor of two when only apertures > 15 arcsec are considered.

Intrinsic variability is almost certainly another factor since many Seyfert galaxies vary in the NIR over timescales of years (e.g., McAlary et al. 1983; Glass 1992; Salvati et al. 1993; Nelson 1996; Glass 1997; Glass 1998), and roughly half of the comparison objects are known or suspected variables (McAlary et al. 1983). Indeed scatter for Seyfert 2s (thought to be less variable than Seyfert 1s, although see Chelli et al. 1987) is between a factor of 1.4 and 2 (in K and J respectively) lower than for both Seyfert types together. Finally, the scatter among the papers we used for comparison (and within them when measurements are conducted over several years) is similar to the scatter between our values and theirs. All things considered, we conclude that 0.1 mag is a conservative upper limit to our NIR photometric errors, and that the NIR photometry is accurate to roughly 0.07 mag, similar to previous work.

4. Elliptical Isophote Fitting

For each galaxy, in each band, isophotes have been fit with ellipses using the STSDAS routine *ellipse* in IRAF. The center coordinates of each galaxy were determined by fitting a two-dimensional Gaussian to the center [shown as (0,0) in Fig. 1]. Then, keeping the center position fixed, brightness profiles were derived in linear radial steps by letting the surface brightness μ, ellipticity $\epsilon = 1 - b/a$, and position angle θ vary with radius. Figure 1 illustrates these profiles (one band per galaxy), as well as the $\sin 4\theta$ and $\cos 4\theta$ residuals of the best-fit ellipse. We have followed the IRAF convention in *ellipse* where A_4 refers to the $\sin 4\theta$ coefficient, and B_4 to $\cos 4\theta$.

Of 64 galaxies with B or V *and* I or J images, 16 appear to suffer from heavy extinction, and the ellipse fits for the shorter wavelengths did not extend over a reasonable radius. In these objects, we have fixed the radial runs of ellipticity and position angle of the shorter wavelength profiles (B or V) to the longer wavelength ones and generated new profiles. These sources are marked in Table 2 with an asterix.

Although an objective procedure, the ellipse fitting may be unduly influenced by bars and spiral structure, and also, in the optical bands, by dust. In those

cases, we might expect values of ellipticity and position angle to differ from those reported in catalogs. A comparison of the ellipticities of the outer regions obtained from the ellipse fitting is shown in Fig. 2, where they are plotted against the equivalent values derived from the axial ratios given in the Third Reference Catalogue of Bright Galaxies (RC3: de Vaucouleurs et al. 1991). The ordinate axis in Fig. 2 shows the mean $< \epsilon >$ over the bands $BVIJ$, or K only when only the K band is available; only the last twenty points in the profile are considered in the calculation of the mean. The error bars correspond to a 1-σ standard deviation over the different bands available. It is evident from the figure that the scatter in the derived ellipticities is rather large; of 76 axial ratios available in RC3, 15 of our measured ellipticities deviate from them by more than 0.2 in either direction (indicated by the dotted lines). Most discrepant ellipticities derived from the images are rounder than those in RC3, implying that spiral structure and bars are not the most important cause of the deviations. Rather, it is likely that their cause is dust extinction, and its incapacitating effect on the ellipse-fitting algorithm. The isophotal values (§5) for these galaxies could be affected by the different ellipse parameters derived by the fitting algorithm, but the availability of multiwavelength data will aid in the determination of the correct values.

5. Isophotal Diameters and Magnitudes in $BVIJHK$

Isophotal levels in the $BVIJHK$ bands were chosen to reflect the noise limits of the observations, but, more importantly, to conform to existing sources of data. Therefore, the B fiducial isophote was defined to be $25\,\mathrm{mag\,arcsec}^{-2}$ in accordance with RC3. The H limit of $21.5\,\mathrm{mag\,arcsec}^{-2}$ is the same as that used in two extensive studies of normal spiral galaxies in the Coma (Gavazzi et al. 1996) and Pisceus-Perseus superclusters (Moriondo et al. 1999). The intervening isophotal limits were defined to follow a smooth trend with log λ: $\mu_{iso}(V) = 24\,\mathrm{mag\,arcsec}^{-2}$, $\mu_{iso}(I) = 23\,\mathrm{mag\,arcsec}^{-2}$, $\mu_{iso}(J) = 22\,\mathrm{mag\,arcsec}^{-2}$, and $\mu_{iso}(K) = 21\,\mathrm{mag\,arcsec}^{-2}$ in K.

The radius R_{band} at a given isophote is the semimajor axis of the fitted elliptical isophote at the isophotal magnitude, and they are reported in Table 2. R_{band} was determined usually by linear interpolation, that is by fitting an exponential to the outer

isophotes. In a minority of cases (32/263), mostly for the apparently large galaxies, extrapolation was necessary to define R since the profile did not reach the level defined by the isophote; these are marked with x in Table 2. Isophotal magnitudes m_{band} were derived by integrating the radial surface brightness profile from the center out to R_{band}, or to the last measured point when R_{band} had to be extrapolated. These values are also given in Table 2.

A comparison of our B-band isophotal parameters and those in RC3 is shown in Fig. 3. The solid lines in both panels correspond to equality, and the dotted lines show the best-fit regression[11] using the ordinary least-squares (OLS) bisector advocated by Isobe et al. (1990). Both diameters and magnitudes are in good agreement with those in RC3, and the fitted regressions are compatible with unit slope. The most discrepant point in the right panel is Mrk 618 which we find more than 2 mag brighter than the RC3 value; its magnitude is derived from an extrapolated value of R_B, and is more than twice as large as those in $VJHK$, which are consistent among themselves and with fainter magnitudes. The next most discrepant point is Mrk 463 (see footnote), 1.5 mag fainter than the RC3 value, and the magnitude is also derived from an extrapolated R_B.

5.1. Trends With Isophotal Diameters and Colors

Figure 4 illustrates the comparison of our isophotal diameters in $VIJK$ with those in B from RC3. As in Fig. 3, the solid lines correspond to equality, and the dotted lines show the best-fit regression. In V, I, and K, the best-fit slopes are less than one, (0.75 in V, 0.81 in K, and 0.89 in I), but in J the fitted slope (1.02) is approximately unity. The less-than-unit slopes in V, I, and K are expected when the corresponding colors in the outer regions ($B-V$, $B-I$, $B-K$) are bluer than the difference in the fiducial isophotes [$(\mu_B - \mu_V)_{iso} = 1$, $(\mu_B - \mu_I)_{iso} = 2$, $(\mu_B - \mu_K)_{iso} = 4$]. This finding implies that colors of Seyfert disks are similar to those of normal early-type spirals, since De Jong (1996) reports integrated early-type spiral colors of $B-V = 0.78$, $B-I = 1.81$, and $B-K = 3.65$.

---

[11] Having eliminated the outlier Mrk 463 from the diameter relation, since it has double nuclei, does not appear to be well-approximated by the ellipse fitting, and is an extrapolated value.

We can further investigate the colors of the outer regions by comparing the ratios of diameters in two different bands to the integrated isophotal color. Such comparisons are shown in Fig. 5a. The solid curves in all panels represent an exponential disk with total disk luminosity given by the isophotal magnitudes, and the central color (difference in disk central surface brightness μ_d in the two bands) given by the difference in the fiducial isophotes. When this last is true, the ratio of the isophotal diameters is equal to the disk scale-length ratio, and this ratio, in principle, depends only on the total color. The previous paragraph demonstrated, however, that for $B - V$, $B - I$, and $B - K$, the outer colors tend to be bluer than the difference in the fiducial isophotes. In this case, the ratio of the isophotal diameters becomes a complicated function of disk scale-length ratio and central color. Either way, Fig. 5a shows that $B - I$ and $B - V$ have a relatively small scatter, and are consistent with integrated colors of normal early-type spirals. An examination of the mean isophotal colors confirms this with $< B - V > = 0.71 \pm 0.45$, $< B - I > = 1.85 \pm 0.42$. The optical–NIR colors, on the other hand, show a larger spread and tend to be redder than those expected for normal spirals ($< B - K > = 4.23 \pm 0.85$), in contrast with what we inferred in the previous paragraph.

Because the isophotal magnitudes we measure also contain the active nucleus and the bulge, assuming that they reflect only an exponential disk is incorrect. Active nuclei and bulges are both "red" contributions to $V - K$ and $J - K$, and would be expected to pull the isophotal colors to the right in Fig. 5. For example, a normal disk should have $V - K$ colors of ≈ 3.0, but almost all the isophotal colors shown in the upper left panel of Fig. 5a are redder than this, although they follow the general trend shown by the solid curve. The data in both upper panels of Fig. 5a also show a larger dispersion than the lower panels. Both of these considerations suggest that, relative to the disk, the emission from the active nucleus+bulge is more significant *and* redder at wavelengths longer than $1\,\mu$m than in the optical.

We can verify the validity of such a claim by subtracting the central flux from the isophotal magnitude, since the "red" contribution is confined to the inner regions. This has been done using the 10-arcsec aperture photometry reported in Table 2, and the resulting plots are shown in Fig. 5b. Although the 10-arcsec flux is only a crude estimate of the active

nucleus+bulge, Fig. 5b supports the hypothesis that their contribution relative to the disk is stronger and redder at longer wavelengths. In the optical bands, the scatter is similar to the photometry before subtraction, but in the NIR, the data after subtraction follow the exponential disk prediction very well, and the scatter relative to it is reduced significantly.

6. Exponential Surface Brightnesses in B and K

The surface brightness of Seyfert disks has been the subject of some controversy. By fitting an exponential to the radial profiles, Yee (1983) tentatively concluded that Seyfert disks were brighter than normal spirals, although noted that selection effects and problems with nuclear subtraction could be responsible for the difference. With a modified version of the same method, similar to what we have done here (see below), MacKenty (1990) found no such difference in disk surface brightness. With two-dimensional NIR bulge+disk+nucleus decompositions Hunt et al. (1999) found that, for a given disk radius, Seyfert disks were almost 1 mag/arcsec^2 brighter at $2\,\mu$m than their normal counterparts, more similar to bulges than to ordinary spiral disks.

Because of this disagreement regarding the properties of Seyfert disks, we discuss briefly the disk surface brightnesses obtained by fitting an exponential to the outer isophotes. (This is the same fit used to determine the isophotal parameters, as described in §5.) However, as pointed out by Mihalas & Binney (1981), the bulge contribution is nonnegligible even at large radii, making the slope of the derived disk component smaller than the slope of the tangent to the galaxy profile. Moreover, one-dimensional profile decomposition can be inaccurate even when the bulge is included in the fit (Byun & Freeman 1995). In spite of these caveats, we have reported the surface brightnesses derived in this way in Table 2 (Col. 11); they have not been corrected for inclination, and should be considered rough estimates (± 0.5 mag).

We have compared the Seyfert surface brightnesses with those of normal spirals taken from de Jong (1996)[12]. The mean surface brightnesses of the two samples[13] are: 21.44 B- and 17.48 K-mag/arcsec^2 for normal spirals, and 20.51 B- and 16.80 K-mag/arcsec^2

---

[12] Also not corrected for inclination.

[13] Over objects with well-defined morphological types.

9

for the Seyferts. The normal value is averaged only over the spiral types present in the Seyfert sample ($T \le 5$) (see below). Figure 6 shows the surface brightnesses in B and K plotted against morphological type T; Seyferts are shown as filled symbols (1s as circles, 2s as squares) and normal spirals by ×s. The sample means are shown by dotted (Seyferts) and dashed (normal) lines in the figure. We have plotted the surface brightnesses as a function of T since there is some indication that, at least in K, disks increase in surface brightness going from late- (Sbc-Sc) to early (Sa-Sab) types (de Jong 1996; Hunt et al. 1999; Moriondo et al. 1999, in preparation). This could be a critical point since Seyferts are usually early types, and, if compared to all spiral types or later ones, their disks could appear to be brighter simply because of their Hubble type.

In any case, Seyfert disks appear to be brighter in both B and K than those in normal spirals of similar morphological type. A formal comparison of the means and spreads (shown in Fig. 6) gives a probability in both bands of $> 99.9\%$ that the two samples are distinct. This result is clearly not conclusive because of the caveats outlined above, and will be the subject of a future paper based on two-dimensional bulge+disk+nucleus decompositions.

7. Summary

We have presented 263 optical and NIR images for 42 Seyfert 1s and 48 Seyfert 2s, selected from the Extended $12\,\mu$m Galaxy Sample. Judging from comparison with previous work, the aperture photometry derived from the images is accurate to roughly $0.05\,$mag in the optical, and $0.07\,$mag in the NIR. B-band isophotal magnitudes and radii, obtained from ellipse fitting, are in good agreement with those of RC3. When compared with the B band, V, I, J, and K isophotal diameters show that the colors in the outer regions are consistent with the colors of normal spirals, in accordance with previous studies. Differences in the integrated isophotal colors and comparison with a simple model show that, relative to the disk, the active nucleus+ bulge emission is larger and redder at longer wavelengths. Finally, roughly estimated Seyfert disk surface brightnesses are significantly brighter than those in normal spirals of similar morphological type.

Future work based on this image atlas includes: 1) an analysis of the radial runs of ellipticity, posi-

tion angle, and quadrupole terms for a quantitative determination of bar and lens properties in Seyferts; 2) two-dimensional decomposition into bulge, disk, and active nucleus; and 3) an analysis of the color images with particular emphasis on the long-wavelength leverage color $V - K$, for which we have the most sources.

REFERENCES

Adams, T.F. 1977, ApJS, 33, 19

Alonso-Herrero, A., Ward, M.J., & Kotilainen, J.K. 1996, MNRAS, 278, 902

Balzano, V.A., & Weedman, D.W. 1981, ApJ, 243, 756

Bessell, M.S., & Brett, J.M. 1988, PASP, 100, 1134

Byun, Y.I., & Freeman, K.C. 1995, ApJ, 448, 563

Casali, M. M. & T. G. Hawarden 1992, JCMT-UKIRT Newsletter, No. 4, p. 33

Chelli, A., Cruz-Gonzalez, I., Carrasco, L., Perrier, C. 1987, A&A, 177, 51

Danese, L., Zitelli, V., Granato, G.L., Wade, R., De Zotti, G., & Mandolesi, N. 1992, ApJ, 399, 38

de Jong, R.S. 1996, A&A, 313, 45

de Jong, R.S. 1996, A&A, 313, 377

de Vaucouleurs, G., de Vaucouleurs, A., Corwin, H. G., Buta, R., Paturel, G., & Fouqué, P. 1991, Third Reference Catalogue of Bright Galaxies (Springer, New York) (RC3)

Elias, J.H., Frogel, J.A., Matthews, K., & Neugebauer, G. 1981, AJ, 87, 1029

Glass, I.S. 1992, MNRAS, 256, 23

Glass, I.S. 1997, MNRAS, 292, 50

Glass, I.S. 1998, MNRAS, 297, 18

Gavazzi, G., Pierini, D., Baffa, C., Lisi, F., Hunt, L.K., Randone, I., & Boselli, A. 1996, A&AS, 120, 521

Granato, G.L., Zitelli, V., Bonoli, F., Danese, L., Bonoli, C., & Delpino, F. 1993, ApJS, 89, 35

Heckman, T.M. 1978, PASP, 90, 241

Ho, L., Filippenko, Al, & Sargent, W. 1997, ApJ, 487, 591

Hunt, L.K., & Giovanardi, C. 1992, AJ, 104, 1018

Hunt, L., Lisi, F., Testi, L., Baffa, C., Borelli, S., Maiolino, R., Moriondo, G., & Stanga, R. M. 1996, A&AS, 115, 181

Hunt, L.K., Malkan, M.A., Salvati, M., Mandolesi, N., Palazzi, E., & Wade, R. 1997, ApJS, 108, 229

Hunt, L. K., Mannucci, F., Testi, L., Migliorini, S., Stanga, R. M., Baffa, C., Lisi, F., & Vanzi, L. 1998, AJ, 115, 2594

Hunt, L.K., Malkan, M.A., Moriondo, G., & Salvati, M. 1999, ApJ, 510, 637

Hunt, L.K. & Malkan, M.A. 1999, ApJ, in press (May) (Paper I)

Isobe, T., Feigelson, E.D., Akritas, M.G., & Babu, G.J. 1990, ApJ, 364, 104

Kotilainen, J.K., Ward, M.J., Boisson, C., DePoy, D.L., Bryant, L.R., & Smith, M.G. 1992a, MNRAS, 256, 125

Kotilainen, J.K., Ward, M.J., Boisson, C., DePoy, D.L., & Smith, M.G. 1992b, MNRAS, 256, 149

Kotilainen, J.K., & Ward, M.J. 1994, MNRAS, 266, 953

Kotilainen, J.K., Ward, M.J., & Williger, G.M. 1993, MNRAS, 263, 655

Landolt, A. U. 1983, AJ, 88, 439

Landolt, A. U. 1992, AJ, 104, 340

Lisi, F., Baffa, C., Biliotti, V., Bonaccini, D., Del Vecchio, C., Gennari, S., Hunt, L.K., Marcucci, G., & Stanga, R. 1996, PASP, 108, 364

MacKenty, J.W. 1990, ApJS, 72, 231

Maiolino, R., Ruiz, M., Rieke, G.H., & Papadopoulos, P. 1997, ApJ, 485, 552

Maiolino, R., Alonso-Herrero, A., Anders, S., Quillen, A., Rieke, G.H., Tacconi-Garman, L.E. 1998, Advances in Space Research, in Proceedings of 32nd Sci. Ass. of COSPAR

McAlary, C.W., McLaren, R.A., McGonegal, R.J., & Maza, J. 1983, ApJS, 52, 341

McLeod, K.K. & Rieke, G.H. 1995, ApJ, 441, 96

Mihalas, D. & Binney, M. 1981, Galactic Astronomy, (San Francisco: Freeman)

Moorwood, A., Finger, G., Biereichel, P. DeLabre, B., Van Dijsseldonik, A. Huster, G., Lizon, J.-L., Meyer, M., Gemperlein, H., & Moneti, A. 1992, The ESO Messenger, 69, 61

Moriondo, G., Baffa, C., Casertano, S., Chincarini, G., Gavazzi, G., Giovanardi, C., Hunt, L.K., Pierini, D., Sperandio, M., & Trinchieri, G. 1999, A&AS, in press

Mulchaey, J.S., & Regan, M.W. 1997, ApJ, 482, L135

Nelson, B.O. 1996, ApJ, 465, 87

Nelson, B.O., McLean, I.S., Henriquez, F., & Magnone, N. 1997, PASP, 109, 600

Peletier, R.F., Knapen, J.H., Shlosman, I., Pèrez-Ramırez, D., Nadeau, D., Doyon, R., Rodriguez Espinosa, J.M., & Pèrez-Garcıa, A.M. 1999, ApJS, in press

Rush, B., Malkan, M.A., & Spinoglio, L. 1993, ApJS, 89, 1

Salvati, M., Hunt, L.K., Calamai, G., et al. 1993, A&A, 274, 174

Sersic, J.L. 1973, PASP, 85, 103

Sersic, J.L. & Pastoriza, M. 1967, PASP, 79, 152

Simkin, S.M., Su, H.J., & Schwarz, M.P. 1980, ApJ, 237, 404

Schild, R., Tresch-Fienberg, R., & Huchra, J. 1985, AJ, 90, 441

Shlosman, I., Frank, J., & Begelman, M.C. 1989, Nature, 338, 45

Shlosman, I., Begelman, M.C., & Frank, J. 1990, Nature, 345, 679

Spinoglio, L., Malkan, M.A., Rush, B., Carrasco, L., & Recillas-Cruz, E. 1995, ApJ, 453, 616

Su, H.J., & Simkin, S.M. 1980, ApJ, 238, L1

Winkler, H., Glass, I.S., van Wyk, F., Marang, F., Spencer Jones, J.H., Buckley, D.A.H., & Sekiguchi, K. 1992, MNRAS, 257, 659

Winge, C., Peterson, B.M., Pastoriza, M.G., Storchi-Bergmann, T. 1996, ApJ, 469, 648

Yee, H.K.C. 1983, ApJ, 473, 473

Zitelli, V., Granato, G.L., Mandolesi, N., Wade, R., & Danese, L. 1993, ApJS, 84, 185
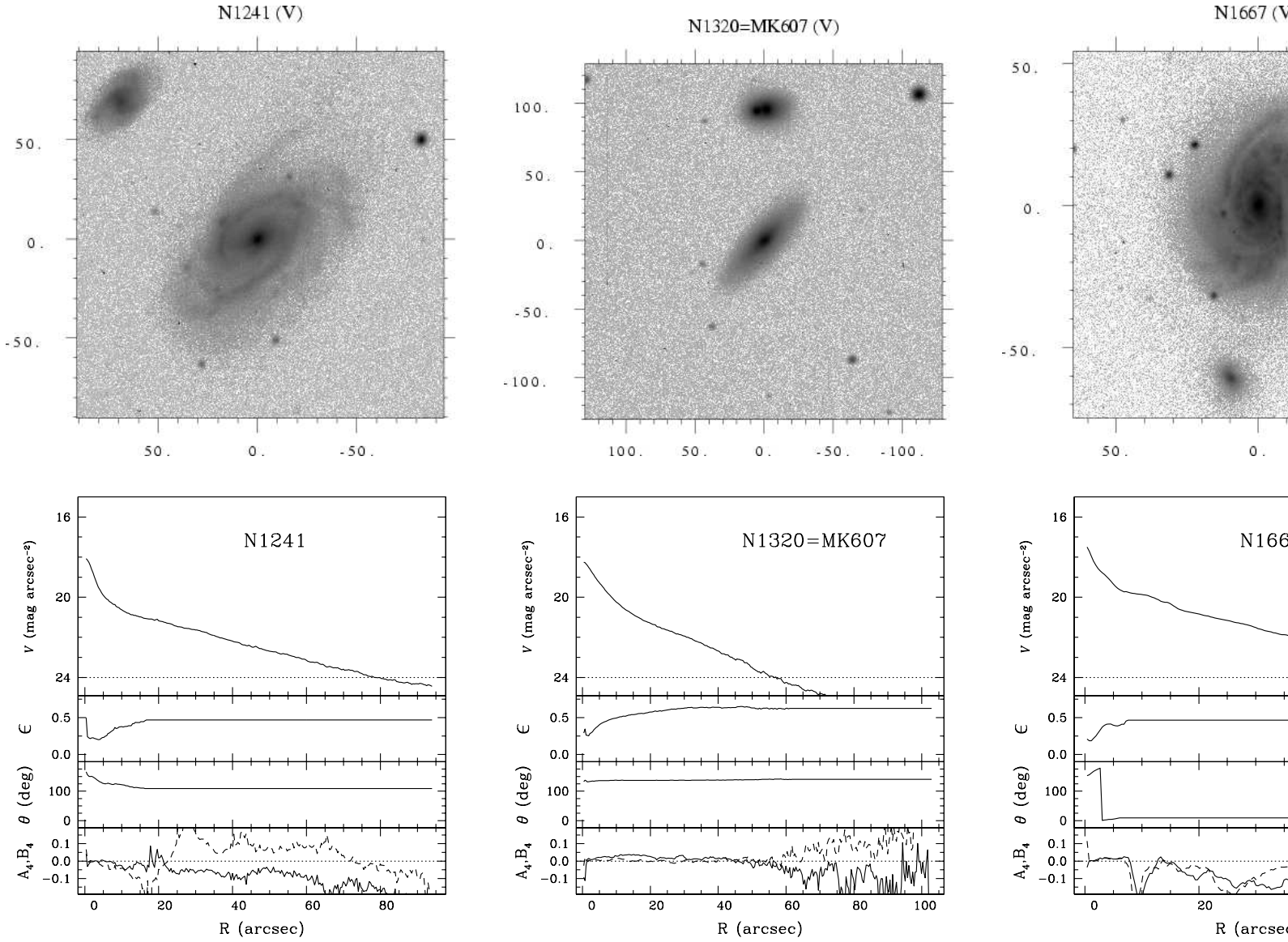
Fig. 1.— Images and profiles (in V, I, J, or K) of 90 12 μm Seyferts, ordered in alphabetical order by name. Images are in units of magnitudes/arcsec^{-2}, with grey scales of 18.5 to 26.5 in B, 18 to 26 in V, 17 to 25.5 in I, 16 to 23.5 in J, and 14.5 to 21.5 in K. North is up, and East is the the left; offsets are in arcsec from the nominal center, also used for profile extraction. The lower panel for each galaxy shows the radial brightness profile, together with the radial runs of ellipticity, position angle, and the sin 4θ coefficient A_4 (dashed line) and cos 4θ coefficient B_4 (solid line). In the topmost of the lower panels, a dotted line shows fiducial isophotal levels, and in the lowermost, the nominal zero level. Shown here are representative examples only.
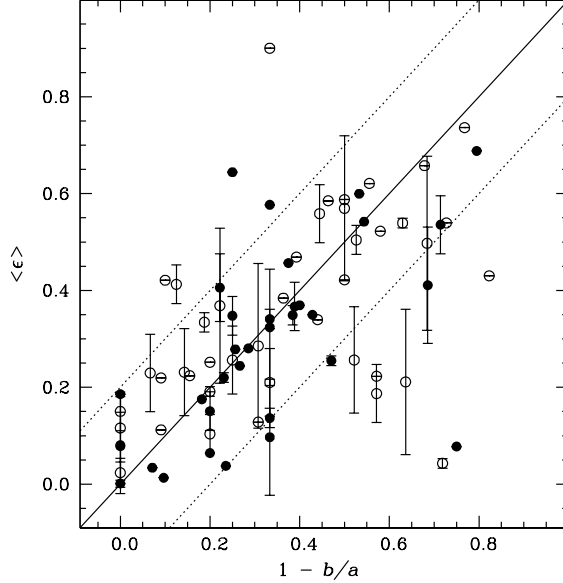
Fig. 2.— The mean ellipticity measured over B, V, I, and J (K only when only band available) bands versus $1 - b/a$ given in RC3. Seyfert 1s are shown by filled circles, and Seyfert 2s by open ones. Error bars are the standard deviation over the bands used in the mean calculation. The solid line shows $< \epsilon > = 1 - b/a$, and the dotted lines enclose the region $| < \epsilon > -(1 - b/a)| > 0.2$.
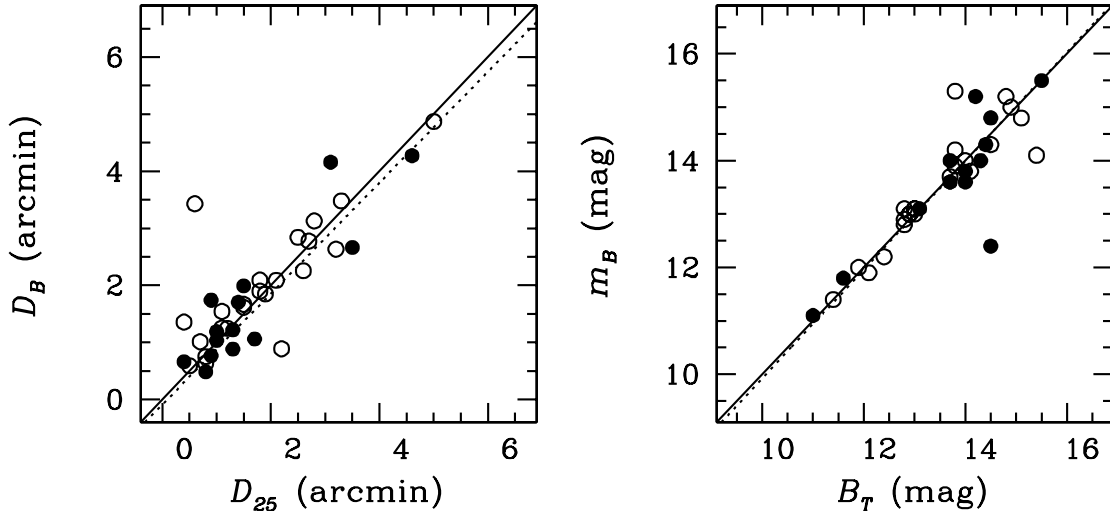
Fig. 3.— Comparison of our B-band isophotal parameters with those from RC3: diameters are shown in the left panel, and magnitudes in the right. Seyfert 1s are shown by filled circles, and Seyfert 2s by open ones. Solid lines in both panels illustrate equality, and the dotted lines show the best-fit regression. The most conspicuous outlier in the left panel is Mrk 463, a double-nuclei galaxy with extrapolated isophotal parameters. The two most conspicuous outliers in the right panel (below and above the best-fit line, respectively) are Mrk 463 and Mrk 618, both with extrapolated radii.

14
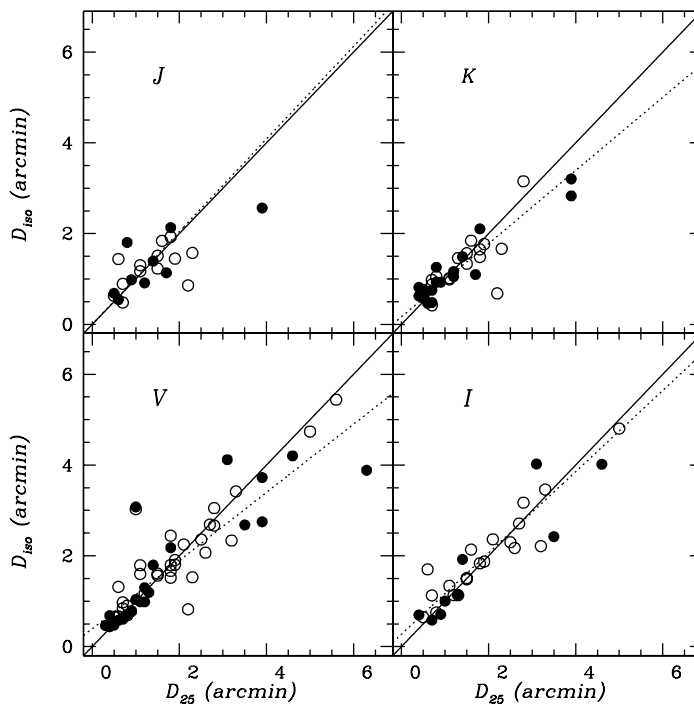
Fig. 4.— Comparison of our $VIJK$-band isophotal diameters with those from RC3. Seyfert 1s are shown by filled circles, and Seyfert 2s by open ones. As in Fig. 3, solid lines correspond to equality, and the dotted lines to the best-fit regression. The less-than-unit slopes in all but the J band imply that the outer colors are bluer than the arbitrary isophotal fiducial magnitude differences listed in the text.
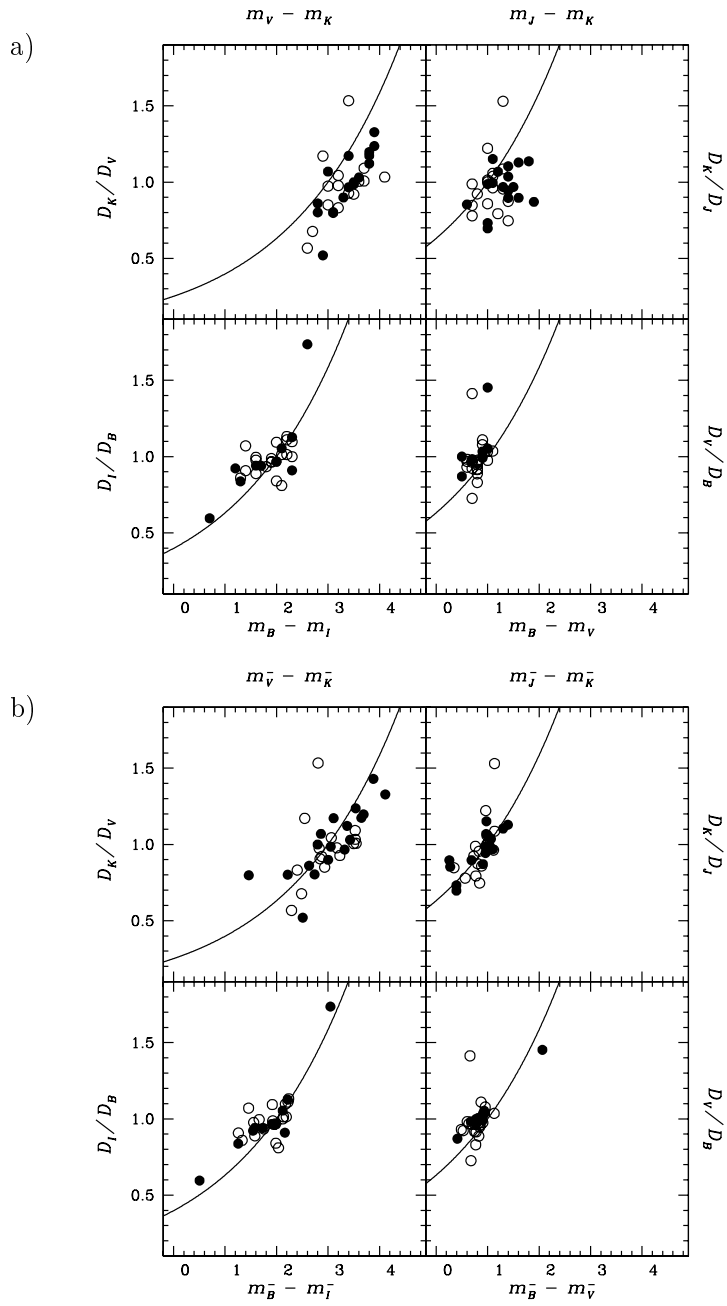
Fig. 5.— Isophotal diameter ratios versus integrated isophotal colors for a restricted set of color combinations. Seyfert 1s are shown by filled circles, and Seyfert 2s by open ones. The solid line illustrates the behavior of a pure exponential disk with the total luminosity given by the isophotal magnitude, and with a central color equal to the difference in the isophotal fiducial magnitudes. Panel a) shows the simple difference of the isophotal magnitudes; panel b) shows the same difference, but after the flux from the central 10 arcsec has been subtracted.
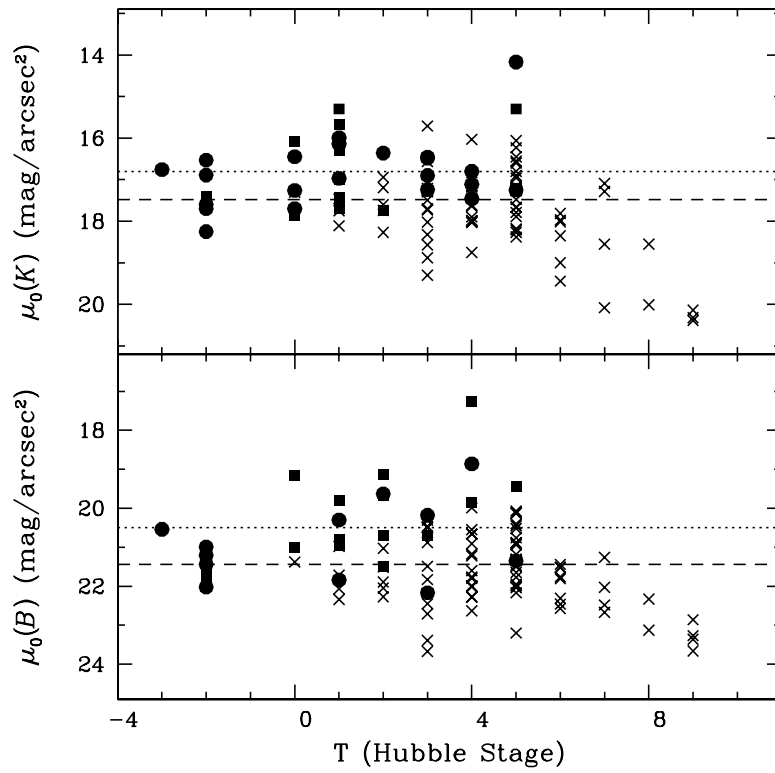
Fig. 6.— The surface brightness μ derived by an exponential fit to the outer profiles plotted against morphological type T. The upper panel shows the K band, and the lower B. Seyfert 1s are shown by filled circles, Seyfert 2s by filled squares, and normal spirals (de Jong citedejong:iii) by ×s. Neither data set has been corrected for inclination. The mean Seyfert surface brightness for the galaxies plotted here (i.e., those with well-defined morphological type) is shown by the dotted lines, and dashed lines show the mean for normal spirals with T $\leq$ 5.

TABLE 2. $12\,\mu$m Seyfert Aperture and Isophotal Photometry

Type (1)	Name (2)	Morph. (3)	z (4)	Band (5)	10" (6)	20" (7)	30" (8)	m_{band} (9)	R_{band} (10)	μ_{disk} (11)	Run (12)
1	3C120	S0:	0.0330	B	15.27	15.18	15.13	15.16	14.5	21.4	E
				V	14.55	14.37	14.26	14.21	21.1	21.0	E
				K	10.74	10.56	10.45	10.31	28.0	17.6	I2
1	3C234		0.1848	K	12.71	12.56	12.45	12.44	22.5	20.5	T
1	3C445		0.0562	J	13.31	13.21	13.15	13.23	9.0	18.9	N
				H	12.23	12.13	12.07	12.13	11.4	18.5	N
				K	11.31	11.27	11.25	11.28	7.9	17.0	N
2	ARP220=UGC09913	S?+Sm	0.0181	J	12.43	11.71	11.41	11.02	36.9	18.1	N
				K	10.84	10.34	10.11	9.74	40.1	17.3	N
2	CGCG381-051		0.0306	J	13.66	12.84	12.46	12.34	22.0	17.3	N
				H	12.95	12.15	11.77	11.64	25.6	17.3	N
				K	12.68	11.96	11.62	11.53	20.3	16.3	N
1	ESO141-G055	S?	0.0360	B	14.41	14.26	14.19	14.02	23.1	21.6	C92
				V	14.04	13.82	13.74	13.51	23.1	21.1	C92
				I	13.40	13.10	12.99	12.82	21.3	19.6	C92
2	ESO541-IG012		0.0566	J	13.35	13.01	12.62	12.14	28.7	19.4	N
				H	12.21	11.98	11.68	11.29	26.8	18.6	N
				K	11.25	11.12	10.95	10.71	21.4	18.1	N
2	F01475-0740	E-S0	0.0177	V	15.97	15.71	15.64	15.73	10.1	20.1	L93
				J	13.74	13.56	13.48	13.59	10.1	18.4	N
				H	12.94	12.77	12.71	12.77	10.9	18.0	N
				K	12.44	12.30	12.24	12.31	15.5	19.2	N
2	F03362-1642		0.0369	B	17.67	17.04	14.18	14.14	19.1	22.1	E
				V	16.39	15.80	13.49	13.45	27.0	20.9	E
				K	11.62	11.38	10.74	10.50	31.7	18.4	I2
1	F03450+0055		0.0310	V	14.69	14.59	14.56	14.59	9.3	19.3	L93
				K	10.75	10.68	10.66	10.68	11.6	16.6	LK
2	F04385-0828	S0	0.0151	V	15.70	15.14	14.95	14.93	19.9	20.0	L93
2	F05189-2524	pec	0.0426	V	16.06	15.72	15.60	15.72	11.0	20.9	E
				I	16.22	15.91	15.79	16.10	6.8	20.3	E
1	F05563-3820		0.0344	V	15.18	14.97	14.90	14.93	18.1	20.4	E
				I	13.80	13.60	13.50	13.52	17.5	18.6	E
				K	11.98	11.82	11.76	11.81	14.5	18.1	I2
1	F07599+6508		0.1488	K	10.38	10.26	10.22	10.20	25.3	18.8	LK
2	F08572+3915		0.0582	V	17.04	16.42	16.24	16.44	11.0	20.7	L93
1	F13349+2438		0.1076	K	10.60	10.44	10.41	10.42	13.3	15.5	LK
1	F15091-2107*		0.0446	B	16.00	15.74	15.52	15.50	19.8	22.3	C92
				V	15.10	14.81	14.61	14.59	20.5	21.4	C92
				I	13.96	13.66	13.48	13.43	20.9	20.1	C92
				K	11.30	11.06	10.93	10.83	24.5	18.3	LK
2	F19254-7245		0.0617	B	17.39	16.60	16.27	16.28	17.2	21.5	C92
				V	16.37	15.61	15.29	15.32	17.8	20.5	C92
				I	14.92	14.26	13.98	13.99	18.9	19.1	C92
2	F22017+0319		0.0611	J	13.48	13.17	13.03	13.06	14.4	18.8	N
				H	12.77	12.48	12.35	12.39	14.1	17.9	N
				K	11.97	11.79	11.72	11.73	12.6	17.5	N
1	IC4329A	SA0+:sp	0.0161	B	14.84	14.48	14.28	13.83	51.1	21.0	C92
				V	13.77	13.42	13.23	12.84	53.8	20.3	C92
				I	12.31	12.02	11.85	11.48	57.7	19.1	C92
2	IC5063	SA(s)0+:	0.0113	B	15.16	14.39	13.99	13.02	62.6	21.5	C92
				V	14.10	13.36	12.98	12.05	67.5	20.8	C92
				I	12.77	12.03	11.66	10.76	70.9	19.5	C92

Table 2. (continued)

Type (1)	Name (2)	Morph. (3)	z (4)	Band (5)	10" (6)	20" (7)	30" (8)	m_{band} (9)	R_{band} (10)	μ_{disk} (11)	Run (12)
1	IZw001	S?	0.0611	V	14.25	14.12	14.03	14.04	14.2	20.3	L93
				J	12.30	12.16	12.06	12.06	15.8	18.5	N
				H	11.35	11.23	11.15	11.14	17.1	17.9	N
				K	10.59	10.52	10.48	10.49	14.2	17.1	N
2	MCG+00-29-023	SAB(s)b	0.0249	B	16.20	15.62	15.38	15.25	22.6	20.7	C92
				V	15.17	14.66	14.44	14.36	20.6	19.6	C92
				I	13.67	13.22	13.05	12.94	22.6	18.7	C92
2	MCG-02-40-004=NGC5995		0.0252	B	15.39	14.86	14.59	14.35	30.4	20.9	C92
				V	14.44	13.92	13.68	13.46	29.2	20.0	C92
				I	13.05	12.56	12.33	12.08	33.8	19.3	C92
				K	10.59	10.16	9.97	9.78	29.4	16.1	N
2	MCG-02-08-039	SAB(rs)apec:	0.0296	I	14.23	13.70	13.30	12.85	33.9	19.3	E
				K	11.86	11.37	11.00	10.65^x	43.8^x	17.4^x	N
2	MCG-03-58-007	(R')SAB(s)0/a	0.0315	B	15.62	15.22	14.98	14.96	17.7	19.2	C92
				V	14.79	14.39	14.16	14.11	19.6	19.3	C92
				I	13.68	13.29	13.07	13.03	19.4	18.2	C92
				J	12.47	12.13	11.94	11.91	18.9	17.0	N
				H	11.52	11.23	11.06	11.02	20.6	16.4	N
				K	10.94	10.73	10.62	10.61	18.1	16.1	N
1	MCG-03-07-011	SAB(s)c	0.0337	V	15.37	14.44	13.93	13.48	29.6	19.1	L93
1	MCG-05-13-017	S0/a	0.0126	V	13.98	13.54	13.31	13.14	29.6	19.7	E
				J	11.90	11.50	11.30	11.16	27.4	17.4	I2
				H	11.14	10.76	10.56	10.42	28.2	16.9	I2
				K	10.82	10.45	10.26	10.13	31.6	16.4	I2
1	MCG-06-30-015*	E-S0	0.0077	B	14.96	14.34	14.16	14.02	31.1	20.5	C92
				V	14.07	13.43	13.27	13.36^x	92.3^x	19.5^x	C92
				I	12.87	12.30	12.14	12.03	30.0	18.6	C92
1	MRK0006=IC0450	SAB0+:.	0.0185	J	11.86	11.47	11.29	10.86	54.2	19.4	T
				H	10.99	10.68	10.53	10.36	36.1	17.6	T
				K	10.38	10.14	10.03	9.90	37.8	17.7	T
1	MRK0009	S0pec?	0.0399	V	14.90	14.53	14.40	14.40	15.4	19.6	L93
				K	10.91	10.70	10.61	10.60	17.3	16.5	LK
1	MRK0079	SBb	0.0222	V	13.92	13.64	13.45	13.10	38.9	20.2	L93
				K	10.41	10.17	10.01	9.83	35.0	16.5	LK
1	MRK0231	SA(rs)c?pec	0.0422	B	14.73	14.52	14.39	14.32	26.5	21.4	L90
				I	12.40	12.17	12.04	11.71	46.0	20.4	L90
				K	9.02	8.92	8.88	8.82	32.4	17.2	LK
2	MRK0273*		0.0378	B	15.74	15.20	15.02	14.81	37.5	22.3	L90
				I	14.30	13.79	13.61	13.36	40.2	21.1	L90
1	MRK0335	S0/a	0.0256	V	14.10	13.94	13.89	13.91	13.9	19.9	L93
				J	12.26	12.16	12.12	12.15	12.4	18.2	N
				H	11.14	11.07	11.04	11.05	13.7	17.9	N
				K	10.87	10.82	10.80	10.83	11.1	17.3	N
2	MRK0463		0.0497	B	15.81	15.13	14.93	15.29^x	102.9^x	20.6^x	L90
1	MRK0509		0.0344	J	11.87	11.73	11.65	11.61	20.5	18.6	N
				H	11.06	10.92	10.84	10.78	22.1	18.0	N
				K	10.16	10.06	10.01	9.96	23.1	17.8	N
1	MRK0618	SB(s)bpec	0.0355	B	13.36	12.81	12.59	12.40^x	52.2^x	20.2^x	L90
				V	14.81	14.35	14.12	14.04	23.8	18.7	E
				J	12.85	12.35	12.12	11.98	29.5	18.4	I2
				H	11.92	11.46	11.24	11.03	35.5	17.9	I2
				K	11.03	10.75	10.61	10.55	27.8	16.9	I2
1	MRK0704	S	0.0299	V	14.52	14.26	14.14	14.13	19.2	19.8	L93
				K	10.62	10.44	10.35	10.30	22.5	16.6	LK

TABLE 2. (continued)

Type (1)	Name (2)	Morph. (3)	z (4)	Band (5)	10" (6)	20" (7)	30" (8)	m_{band} (9)	R_{band} (10)	μ_{disk} (11)	Run (12)
1	NGC4253=MRK766	(R')SB(s)a:	0.0129	B	14.65	14.13	13.87	13.55	35.7	20.3	L90
				V	14.11	13.62	13.37	13.09	31.1	19.3	L93
				I	13.41	12.87	12.59	12.30	29.9	18.5	L90
				J	11.97	11.51	11.28	11.04	29.6	16.8	T
				H	10.98	10.60	10.41	10.18	30.8	16.2	T
				K	10.10	9.86	9.72	9.56	30.6	16.1	T
1	MRK0817	S?	0.0315	K	10.49	10.27	10.16	9.90	31.9	18.1	LK
2	NGC0034=MRK0938	Pec	0.0198	B	14.96	14.32	14.10	13.96	26.7	19.9	E
				V	14.21	13.64	13.45	13.34	24.6	19.4	E
				J	11.88	11.55	11.42	11.34	25.8	18.4	I2
				H	10.95	10.70	10.61	10.56	22.3	17.2	I2
				K	10.46	10.24	10.17	10.13	20.5	16.8	I2
1	MRK1034	S?	0.0338	V	15.11	14.65	14.49	14.48	17.4	19.5	L93
				J	12.76	12.40	12.28	12.29	16.4	17.1	N
				H	11.99	11.63	11.51	11.50	17.1	16.4	N
				K	12.03	11.72	11.66	11.70	14.0	15.8	N
1	MRK1239	E-S0	0.0199	V	14.82	14.43	14.36	14.38	13.2	18.4	L93
				K	9.54	9.44	9.41	9.40	18.8	16.8	LK
2	NGC0262=MRK0348	SA(s)0/a:	0.0151	V	14.88	14.29	14.00	13.15	53.8	21.8	L93
				J	12.52	12.01	11.76	11.26	39.2	19.1	N
				H	11.81	11.31	11.06	10.55	40.5	18.4	N
				K	11.57	11.12	10.89	10.56	30.5	17.9	N
2	NGC0424*	(R)SB(r)0/a	0.0117	B	15.40	14.68	14.29	13.74^x	56.9^x	21.0^x	E
				V	14.49	13.78	13.39	12.88	53.9	20.1	E
				I	13.38	12.63	12.25	11.75	55.0	19.0	E
2	NGC0513	S?	0.0195	V	14.59	13.74	13.48	13.37	25.3	17.2	L93
				J	11.96	11.26	11.04	10.95	26.8	15.1	N
				H	11.45	10.77	10.56	10.49	25.6	14.3	N
				K	11.13	10.46	10.25	10.16	26.4	14.7	N
1	NGC0526A	S0pec?	0.0192	B	15.85	15.40	15.19	14.79	31.8	22.0	E
				J	12.42	12.10	11.95	11.61	34.0	19.3	I2
				H	11.40	11.15	11.04	10.84	29.0	18.6	I2
				K	10.58	10.41	10.32	10.13	32.9	18.2	I2
1	NGC0931=MRK1040*	Sbc	0.0167	V	14.83	14.18	13.81	12.86^x	82.5^x	20.9^x	L93
				J	12.27	11.64	11.30	10.65^x	77.0^x	18.4^x	N
				H	11.24	10.63	10.29	9.73^x	99.3^x	17.7^x	N
				K	10.69	10.15	9.85	9.28^x	85.0^x	17.1^x	N
2	NGC1056=MRK1183	Sa:	0.0052	V	14.16	13.58	13.30	12.80	45.8	20.4	L93
				J	11.33	10.79	10.56	10.17	47.2	17.8	N
				H	10.44	9.93	9.71	9.35	50.5	17.2	N
				K	10.12	9.62	9.41	9.10	50.0	17.0	N
2	NGC1068=M77	(R)SA(rs)b	0.0038	V	11.31	10.63	10.28	9.01	148.0	20.1	L93
2	NGC1125	(R')SAB(rl:)0$^+$	0.0110	V	14.61	13.88	13.53	13.02	50.0	19.6	L93
2	NGC1143/44*	RingB	0.0288	B	16.20	15.22	14.80	13.93	46.3	21.6	E
				V	14.98	14.12	13.72	12.79	48.0	20.5	E
				J	12.23	11.50	11.19	10.35	50.1	18.4	I2
				H	11.34	10.63	10.34	9.57^x	64.1^x	17.7^x	I2
				K	10.93	10.21	9.95	9.20	48.2	17.8	I2
2	NGC1194	SA0+:	0.0132	V	14.49	13.74	13.39	12.44	73.3	21.2	L93
				J	12.12	11.53	11.24	10.68	57.8	18.6	N
				H	11.31	10.74	10.46	9.95^x	63.0^x	18.0^x	N
				K	10.94	10.44	10.19	9.71	49.6	17.4	N
2	NGC1241	SB(rs)b	0.0135	V	14.55	13.85	13.41	12.23	80.0	20.3	L93

TABLE 2. (continued)

Type (1)	Name (2)	Morph. (3)	z (4)	Band (5)	10" (6)	20" (7)	30" (8)	m_{band} (9)	R_{band} (10)	μ_{disk} (11)	Run (12)
2	NGC1320=MRK0607	Sa:sp	0.0091	V	14.33	13.64	13.33	12.81	57.2	19.8	L93
				J	11.63	11.09	10.83	10.42	43.4	17.4	N
				H	10.84	10.32	10.08	9.68	56.6	16.0	N
				K	10.45	9.97	9.74	9.38	53.0	15.7	N
2	NGC1667	SAB(r)c	0.0152	B	15.22	14.22	13.73	12.93	62.8	19.4	E
				V	14.23	13.37	12.92	12.21	45.6	18.4	E
				K	10.68	9.88	9.49	8.97	44.6	15.3	I2
1	NGC2639	(R)SA(r)a:?	0.0106	V	13.59	12.82	12.45	11.81	65.4	19.5	L93
				J	11.04	10.28	9.92	9.40	64.0	16.8	X
				K	10.04	9.27	8.91	8.44	63.2	16.0	X
1	NGC2992	Sapec	0.0077	B	15.31	14.50	14.02	13.07	79.9	21.8	C92
				V	14.25	13.48	13.04	12.21	80.5	20.9	C92
				I	12.76	12.05	11.68	10.85	72.7	19.9	C92
2	NGC3079	SB(s)c	0.0038	V	14.76	13.51	12.89	10.85	122.1	20.4	L93
1	NGC3227	SAB(s)pec	0.0039	J	10.90	10.42	10.10	8.99^x	125.0^x	17.1^x	X
				K	9.59	9.20	8.92	8.26^x	253.5^x	17.3^x	X
				K	9.46	9.07	8.81	7.24	142.1	17.0	T
1	NGC3516	(R)SB(s)0^0 :	0.0088	K	9.34	8.99	8.82	8.47	51.4	16.9	T
1	NGC4051	SAB(rs)bc	0.0024	J	11.22	10.73	10.42	8.75^x	208.8^x	18.3^x	T
				H	10.38	9.95	9.67	8.07	141.1	17.1	T
				K	9.98	9.61	9.36	7.69^x	207.7^x	17.5^x	T
1	NGC4151	(R')SAB(rs)ab:	0.0033	V	11.88	11.55	11.37	10.57^x	116.6^x	20.4^x	L93
				K	8.36	8.11	7.96	7.65^x	60.6^x	16.4^x	LK
2	NGC4388*	SA(s)b:sp	0.0084	V	14.41	13.38	12.80	11.34^x	163.2^x	20.2^x	CA
				I	13.10	12.05	11.51	10.18^x	155.8^x	19.0^x	CA
2	NGC4501=M88	SA(rs)b	0.0076	I	11.68	10.83	10.37	8.57^x	350.9^x	19.1^x	CA
1	NGC4593	(R)SB(rs)b	0.0090	V	13.85	13.03	12.65	11.24	111.8	20.2	L93
				K	10.04	9.48	9.20	8.43^x	96.2^x	16.5^x	LK
2	NGC4968	(R')SAB0^0	0.0099	B	15.80	15.13	14.83	14.17	55.5	21.8	C92
				V	14.79	14.15	13.86	13.24	54.1	20.9	C92
				I	13.52	12.90	12.62	11.96	56.2	19.8	C92
1	NGC5033	SA(s)c	0.0029	K	9.28	8.54	8.20	7.58^x	76.2^x	14.2^x	LK
2	NGC5135	SB(l)ab	0.0137	B	14.34	13.88	13.62	12.97	67.7	20.7	C92
				V	13.69	13.17	12.88	12.25	62.1	19.6	C92
				I	12.62	12.05	11.74	11.08	65.2	18.6	C92
2	NGC5256=MRK0266	pec	0.0279	B	15.53	14.61	14.19	13.85^x	40.7^x	20.9^x	L90
				I	14.21	13.33	12.93	12.52	35.0	19.8	L90
2	NGC5506*	Sapec	0.0062	B	15.84	14.90	14.42	13.12	93.9	19.8	C92
				V	14.89	13.96	13.48	12.26	91.6	19.1	C92
				I	13.55	12.66	12.18	10.97	95.2	17.4	C92
				K	8.98	8.80	8.67	8.15	94.6	15.3	T
1	NGC5548	(R')SA(s)0/a	0.0172	J	11.73	11.26	11.02	10.58	41.8	18.4	T
				K	10.24	9.92	9.75	9.40	44.7	17.7	T
2	NGC5929*	Sab:pec	0.0083	V	14.49	13.87	13.51	11.86^x	90.8^x	20.7^x	CA
				I	13.19	12.59	12.27	10.82	77.5	19.3	CA
				J	12.04	11.54	11.27	9.88	76.2	18.6	N
				H	11.29	10.80	10.53	9.16^x	84.4^x	17.9^x	N
				K	11.05	10.58	10.32	8.87^x	77.2^x	17.7^x	N
2	NGC5953	SAa:pec	0.0066	I	12.19	11.66	11.46	10.66	64.1	19.6	CA
				J	11.23	10.73	10.54	9.85	55.2	18.4	N
				H	10.39	9.91	9.73	9.08	58.0	17.7	N
				K	10.20	9.70	9.53	8.85	55.3	17.7	N
2	NGC6810	SA(s)ab:sp	0.0068	B	14.54	13.77	13.36	12.25	79.0	21.5	C92
				V	13.54	12.78	12.38	11.40	70.1	20.3	C92
				I	12.12	11.38	11.02	10.20	66.4	18.8	C92

TABLE 2. (continued)

Type (1)	Name (2)	Morph. (3)	z (4)	Band (5)	10" (6)	20" (7)	30" (8)	m_{band} (9)	R_{band} (10)	μ_{disk} (11)	Run (12)
1	NGC6860	(R')SB(r)ab	0.0149	B	14.85	14.25	13.94	13.64	36.6	19.6	C92
				V	14.05	13.45	13.15	12.86	35.8	19.2	C92
				I	12.98	12.39	12.11	11.86	34.4	18.0	C92
2	NGC6890*	(R')SA(r:)ab	0.0081	B	15.18	14.23	13.75	13.06	48.5	19.7	C92
				V	14.26	13.38	12.94	12.28	46.9	18.9	C92
				I	13.13	12.29	11.86	11.26	45.3	17.6	C92
2	NGC7130=I5135*	Sapec	0.0162	B	14.73	13.85	13.47	12.99	50.1	20.8	C92
				V	14.08	13.22	12.83	12.30	48.3	19.9	C92
				I	13.15	12.33	11.89	11.41	44.5	18.9	C92
				J	11.92	11.16	10.72	10.43^x	45.3^x	17.2^x	I2
				H	11.10	10.38	9.95	9.62^x	38.2^x	16.4^x	I2
				K	10.70	10.01	9.59	9.34^x	47.0^x	16.3^x	I2
2	NGC7172*	Sapec	0.0087	B	15.60	14.77	14.27	12.80	85.2	20.9	C92
				V	14.59	13.76	13.27	12.01	70.8	19.2	C92
				I	13.01	12.20	11.75	10.71	69.0	17.4	C92
1	NGC7213	SA(s)0^0	0.0060	B	13.51	12.74	12.29	11.07^x	124.7^x	21.2^x	C92
				V	12.58	11.82	11.38	10.16^x	123.5^x	20.3^x	C92
				I	11.42	10.67	10.26	9.08^x	120.7^x	19.1^x	C92
1	NGC7314*	SAB(rs)bc	0.0047	B	15.86	14.78	14.14	11.78	128.2	18.9	C92
				V	14.96	13.90	13.29	11.10	126.1	18.8	C92
				I	13.82	12.78	12.20	10.19	120.5	17.9	C92
1	NGC7469	(R')SAB(rs)a	0.0163	J	10.93	10.60	10.42	10.05	48.2	18.6	N
				H	10.10	9.80	9.64	9.31	50.6	18.0	N
				K	9.60	9.39	9.28	9.14	35.3	17.0	N
2	NGC7496*	(R':)SB(rs)bc+SB(s)m	0.0055	B	14.82	14.31	13.95	12.04	104.4	19.9	C92
				V	14.28	13.69	13.29	11.44	102.5	19.7	C92
				I	13.34	12.67	12.25	10.39	103.9	18.6	C92
2	NGC7582*	(R'$_1$)SB(s)ab	0.0053	B	14.68	13.96	13.46	11.44	146.1	19.1	C92
				V	13.79	13.06	12.58	10.66	142.2	18.4	C92
				I	12.36	11.68	11.24	9.49	144.2	17.3	C92
2	NGC7590*	S(r?)bc	0.0053	B	14.88	13.87	13.30	11.95	83.3	17.3	C92
				V	13.95	13.06	12.56	11.29	80.6	17.7	C92
				I	12.72	11.94	11.49	10.34	81.3	17.3	C92
1	NGC7603=MRK0530	SA(rs)b:pec	0.0295	B	15.15	14.72	14.45	13.55	59.7	22.2	L90
				I	14.15	13.61	13.31	12.91	35.5	20.0	L90
				J	11.85	11.39	11.15	10.73	44.6	18.1	N
				H	10.88	10.49	10.28	9.90	46.5	17.4	N
				K	10.20	9.91	9.75	9.40	43.2	17.2	N
2	NGC7674=MRK0533	SA(r)bcpec	0.0291	J	12.51	11.87	11.54	10.98	35.1	17.7	N
				H	11.67	11.07	10.76	10.17	36.1	16.9	N
				K	11.18	10.77	10.55	10.30	29.8	16.8	N
2	TOL1238-364=IC3639	SB(rs)bc:S	0.0110	B	14.65	13.99	13.60	13.07	37.5	18.4	C92
				V	13.92	13.31	12.97	12.52	34.9	18.0	C92
				I	12.98	12.40	12.10	11.70	34.0	17.9	C92
2	UGC11680=MRK0897		0.0263	V	15.13	14.86	14.73	14.75	39.4	22.7	CA
				I	14.01	13.68	13.51	13.36	51.0	22.0	CA
				J	12.79	12.55	0.00	11.82	43.2	20.9	N
				H	12.12	11.86	11.75	11.17	52.5	20.5	N
				K	11.90	11.69	0.00	11.62	35.7	19.8	N

*Sources for which B and V profiles extracted with I-or J-band ellipse parameters.
^{x}Isophotal radius is extrapolated, not interpolated.